



Title	Model building analysis : a novel method for statistical evaluation of Pt L3-edge EXAFS data to unravel the structure of Pt-alloy nanoparticles for the oxygen reduction reaction on highly oriented pyrolytic graphite
Author(s)	Feiten, Felix E.; Takahashi, Shuntaro; Sekizawa, Oki; Wakisaka, Yuki; Sakata, Tomohiro; Todoroki, Naoto; Uruga, Tomoya; Wadayama, Toshimasa; Iwasawa, Yasuhiro; Asakura, Kiyotaka
Citation	Physical chemistry chemical physics, 22(34), 18815-18823 https://doi.org/10.1039/c9cp06891k
Issue Date	2020-09-14
Doc URL	http://hdl.handle.net/2115/82650
Type	article (author version)
File Information	Feiten_2019.pdf



[Instructions for use](#)

Cite this: DOI: 00.0000/xxxxxxxxxx

Model Building Analysis - a novel method for statistical evaluation of Pt L₃-edge EXAFS data to unravel the structure of Pt-alloy nanoparticles for the oxygen reduction reaction on highly oriented pyrolytic graphite.

Felix E. Feiten,^{a,‡} Shuntaro Takahashi,^b Oki Sekizawa,^{c,d} Yuki Wakisaka,^a Tomohiro Sakata,^c Naoto Todoroki,^b Tomoya Uruga,^{b,d} Toshimasa Wadayama,^b Yasuhiro Iwasawa,^c and Kiyotaka Asakura,^{*a}

Received Date
Accepted Date

DOI: 00.0000/xxxxxxxxxx

Extended X-ray absorption fine structure (EXAFS) is a powerful tool to determine the local structure in Pt nanoparticles (NP) on carbon supports, active catalysts for fuel cells. Highly oriented pyrolytic graphite (HOPG) covered with Pt NP gives samples with flat surfaces that allow application of surface science techniques. However, the low concentration of Pt makes it difficult to obtain good quality EXAFS data. We have performed *in situ* highly sensitive BCLA-empowered Back Illuminated EXAFS (BCLA+BI-EXAFS) measurements on Pt alloy nanoparticles. We obtained high quality Pt L₃-edge data. We have devised a novel analytical method (Model Building Analysis) to determine the structure of multi-component nanoparticles from just a single absorption edge. The generation of large numbers of structural models and their comparison with EXAFS fits allows us to determine the structures of Pt-containing nanoparticles, catalysts for the oxygen reduction reaction. Our results show that PtCo, PtCoN and AuPtCoN form a Pt-shell during electrochemical dealloying and that the ORR activity is directly proportional to the Pt-Pt bond length.

1 Introduction

The ever-increasing demand for energy and the challenges of global warming necessitate the advancement of clean sources of energy. One promising technology, especially as a power source in vehicles, is the polymer electrolyte fuel cell (PEFC). While this type of fuel cell is already commercialized in vehicles, it faces several severe challenges.^{1,2} One of the most critical issues limiting the commercial success of PEFC vehicles so far, is the slow oxygen reduction reaction (ORR) at the fuel cell cathode. Pt nanoparticles (NPs) are commonly used as the catalyst but they show limited stability and are extremely expensive.^{3–8} One approach to reduce the amount of Pt and to enhance the area specific activities in ORR catalysts is the alloying of Pt with other transition metals

such as Co or Ni.^{8–12} However, these bimetallic NPs suffer from very low durability. While Pt is often dissolved slower under reaction conditions, compared to the pure Pt NPs, the less noble metal is leached very quickly. This leads to limited structural stability and eventually the dissolution of Pt.^{6,13–15} Takahashi et al. have demonstrated two different methods to stabilize PtCo bimetallic NPs prepared by arc plasma deposition (APD) on a flat highly oriented pyrolytic graphite (HOPG) sample: 1. Formation of CoN within the PtCo alloy nanoparticles. Codeposition of Pt and Co in a nitrogen atmosphere leads to the inclusion of N into the NPs and the formation of CoN. These N-stabilized PtCo particles show improved stability.¹⁶ 2. Deposition of Au onto Pt nanoparticles. The deposition of Au onto Pt NPs results in preferential occupation of the low-coordination sites, which are most prone to dissolution during the oxygen reduction reaction, in turn stabilizing the particles.¹⁷ Combining these two approaches, AuPtCoN nanoparticles provide higher activity and stability.¹⁸ In order to obtain structural information we conducted *in situ* Extended X-ray Absorption Fine Structure (EXAFS) measurements in solution with an applied potential, comparing the structures of AuPtCoN nanoparticles to those of PtCoN, PtCo and pure Pt particles. However it is impossible to characterize the Pt samples, prepared with APD, by conventional fluorescence EXAFS because APD requires flat sub-

^a Institute for Catalysis, Hokkaido University, Sapporo 001-0021, Hokkaido, Japan.

[‡] Present address: Fritz-Haber-Institut der Max-Planck-Gesellschaft, Department of Interface Science, Faradayweg 4-6, 14055 Berlin, Germany

^b Graduate School of Environmental Studies, Tohoku University, Sendai 980-8579, Japan.

^c Innovation Research Center for Fuel Cells, University of Electro-Communications, Chofu Tokyo 182-8585, Japan.

^d Japan Synchrotron Radiation Research Institute (JASRI), Hyogo 679-5148, Japan

† Electronic Supplementary Information (ESI) available: See DOI: 10.1039/cXCP00000x/

strates like HOPG which have low surface areas, resulting in very small total amounts of Pt ($1 - 2 \times 10^{15} \text{cm}^{-2}$). Moreover, in *in situ* experiments the electrolyte strongly absorbs the incident and fluorescent X-rays and creates a large amount of scattering X-rays, which degrades the XAFS signal significantly. In this work we use back-illuminated X-ray absorption spectroscopy (BI-XAFS) in combination with a bent crystal Laue analyzer (BCLA). BCLA+BI-XAFS allows us to detect EXAFS of very small amounts of Pt on the HOPG surface in the presence of electrolyte. In BI-XAFS, the substrate HOPG plays three roles: 1. X-ray transparent window, 2. support for Pt and its alloy NPs, and 3. working electrode to apply potential to the NPs. The NPs are facing towards the thick solution layer and they are illuminated by X-rays from the back side through the HOPG to prevent undesired X-ray absorption by the electrolyte. Since a large amount of scattering occurs from the solution, we apply a BCLA to filter out all but the fluorescent X-rays of the Pt L_{III} -edge. The BCLA allows measurement of the Pt L_{III} -edge EXAFS without interference from the Au L_{III} -edge. We could measure the high k -region and achieved increased reliability of the EXAFS spectra. Co K -edge EXAFS could not be obtained due to the low signal to noise (S/N) ratio as described below. The EXAFS analysis is limited by a strong correlation between the Debye-Waller factor σ^2 and the coordination number N ^{19,20}, as described in more detail in Section 4.4 and the Supporting Information. In order to break up the correlation we systematically varied the Debye-Waller factors for two scattering paths, Pt-Pt and Pt-Co, in EXAFS fitting to obtain physically reasonable fits by comparing the obtained parameters to those derived from real space structural models. In the rest of the paper we refer to this analysis as model building analysis (MBA). Consequently, we could increase the accuracy of the fitting results. We discuss the increased stability and activity based on the EXAFS analysis and we propose structural models for each nanoparticle. The results of this analysis allow us to 1) determine the Pt-Pt bond length and its correlation with the activity in the oxygen reduction reaction and 2) identify structural models for the different samples.

2 Experimental Details

Nanoparticles were prepared on HOPG by APD (APD sources: ULVAC-RIKO ARL-300). One Pt source was used to deposit pure Pt NPs. Two sources, one Pt and one Co were used to co-deposit both metals simultaneously to form PtCo alloy NPs. N was incorporated by performing the co-deposition of Pt and Co under nitrogen atmosphere of 0.1 Pa, PtCo without N was prepared in ultra-high vacuum (UHV). A Au source was used to deposit Au onto PtCoN particles in UHV to form AuPtCoN. The nanoparticle preparation is described in more detail elsewhere.¹⁶⁻¹⁸ A home-built electrochemical cell for X-ray spectroscopy was used to perform the experiments. Photographs of the cell are shown in Fig. S1 of the Supporting Information (SI). The cell body was made from polychlorotrifluoroethylene (PCTFE). The sample NPs were deposited on a very thin HOPG plate on one side. The HOPG was mounted on the cell with the deposited NPs facing inwards and contacting the solution. The other side was exposed to atmosphere and let the incident X-rays come in as well as the fluorescent X-rays go out as shown in Fig. 2. We refer to this config-

uration as BI or back-illuminated.^{21,22} This configuration avoids x-rays travelling through a thick layer of electrolyte and reduces the absorption from the solution. In addition, the HOPG substrate also acted as the working electrode. An important merit is that the Pt catalyst on the working electrode has good contact with the electrolyte in order to circumvent problems with mass transport in the solution. A difficulty of this BI method is the thickness of the HOPG window. It must be as thin as possible, but too thin windows result in holes and cracks that lead to leakage of the solution. In this work the HOPG thickness was appropriate for Pt L_{III} -edge measurements, but it was too thick for successful Co K -edge measurements as discussed later. A glass window was placed at the other side of the cell to obtain a clear view of the inside. The cell was filled with 0.1 M HClO_4 through an inlet from the bottom. During measurements, the N_2 -purged solution was circulated constantly. The Ag/AgCl reference electrode and Pt counterelectrode were inserted into the cell from the side. These electrodes were covered with Pb sheets to prevent undesired fluorescence from these Pt electrodes. Scanning Transmission Electron Microscopy (STEM) and STEM-Energy Dispersive X-ray Spectrometry (EDS) measurements were performed on a JEOL JEM-ARM200F as described elsewhere.¹⁶⁻¹⁸

EXAFS measurements were performed at beamline BL36XU at SPring-8 (Super Photon ring - 8 GeV, JASRI, Japan). Fluorescence X-rays were collected by a 25-element Ge solid state detector (SSD). A BCLA was used in front of the SSD in order to remove the strong elastic scattering from the solution. Two BCLAs, purchased from Oxford FMB, were used: BCLA0075 for the Co K -edge and BCLA0095 for the Pt L_{III} -edge. Five scans were performed for each sample. During the measurements the sample was held at 0.17 V relative to the Ag/AgCl reference electrode. At this potential the surface is free from adsorbates which allows investigation of the structures of the intact Pt and Pt alloy nanoparticles. To activate the nanoparticle samples, the applied potential was cycled between 0.28 V and 1.28 V versus Ag/AgCl 300 times. This procedure is henceforth referred to as “electrochemical conditioning” or just “conditioning”. Measurements on each sample were performed both before conditioning (bc) and after conditioning (ac). An overview over the resulting spectra can be found in Fig. S2 in the SI. There are spikes in the spectra, caused by the formation of bubbles and their desorption from the sample surface. Their origin is discussed in more detail in the SI and their removal from the spectra is explained in the following section.

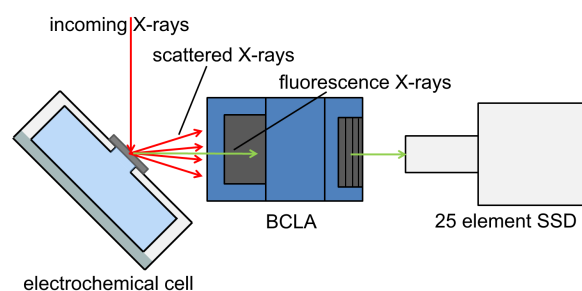


Fig. 1 Scheme of experimental setup

3 Analysis Details

The Athena and Artemis software packages were used to process and analyze EXAFS data.²³ The 25 channels of the SSD were summed up after removing those channels that showed no significant edge-jump. Afterwards, the spikes were removed by replacing the value at each spike with the average of the values before and after the spike. Next, five scans for a measurement were averaged. Background subtraction and normalization were performed on the averaged spectra in the standard way furnished in Athena. Curve fitting analysis for the resulting $\chi(k)$ spectra was performed in Artemis using the EXAFS equation 1:

$$\chi(k) = S_0^2 \sum_j \frac{N_j e^{-2k^2 \sigma_j^2} e^{-2r_j/\lambda(k)} f_j(k)}{kr_j^2} \sin[2kr_j + \delta_j(k)] \quad (1)$$

S_0^2 is the overall reduction factor obtained from two references, Pt foil and Pt₉Co₁ foil; $f_j(k)$, $\delta_j(k)$ and $\lambda(k)$ are the backscattering amplitude, phase shift and inelastic scattering factor, respectively and were calculated with FEFF 6 using a Pt absorber surrounded by 11 Pt atoms and 1 Co atom. N_j , σ_j^2 , r_j are coordination numbers, Debye-Waller factor and bond distance of the j-th shell, respectively and they were used as fitting parameters. The wave number, k , was obtained through the following equation:

$$k = \frac{2m}{\hbar^2} \sqrt{\hbar\omega - E_0} \quad (2)$$

where E_0 is the origin of the photoelectron kinetic energy. The difference in E_0 between experiment and theoretical calculation, ΔE_0 , used in the software to align energy scales, was fixed to the value of the Pt reference foil in order to reduce the correlation between parameters in the fitting procedure. Fitting was performed on the data back-transformed from r -space with three k -weights, 1, 2 and 3 simultaneously. Analysis was performed with a k -range from 3 Å⁻¹ to 12.25 Å⁻¹ and a range in r from 1.5 Å to 3.25 Å.

4 Results and Discussion

4.1 STEM and EDS

STEM and EDS were performed to determine the average particle diameters and the Pt/Co ratios shown in Table 1. Typical STEM images can be found in Figures S3 to S8 of the SI. The pure Pt NPs coalesce as a result of electrochemical conditioning and thus show an increase in average diameter, despite dissolution of some Pt. All Co-containing samples show a decrease in average particle diameter and an increase in the Pt/Co-ratio as a result of conditioning. These phenomena can be explained by a loss of cobalt, which is partially dissolved during the electrochemical conditioning. The increase in the Pt/Co-ratio is largest for PtCo and smallest for AuPtCoN, both absolutely as well as relatively. While all nanoparticles lose some Pt in the electrochemical conditioning, as shown in Table 1 and discussed below, the increased Pt/Co-ratios aC are the result of loss of more Co than Pt. The smallest increase in the Pt/Co-ratio for AuPtCoN indicates the stabilization of Co within these nanoparticles through CoN-formation and Au adatoms. The largest increase in the Pt/Co-ratio for PtCo is due to a lack of stabilization and the resulting significant loss of Co.

The STEM-EDS measurements indicate the formation of Pt-shells as a consequence of electrochemical dealloying and are discussed in detail elsewhere.^{16,18}

Table 1 Average particle diameters, Pt/Co-ratios obtained from STEM-EDS, Pt loss calculated from the decrease in the Pt L_{III}-edge jump

Sample	Average diameter / nm	Pt/Co-ratio	Pt loss / %
Pt bC	4.2 ± 1.5	-	-
Pt aC	4.5 ± 1.6	-	4.5 ± 0.2
PtCo bC	4.8 ± 1.9	1.7 ± 0.3	-
PtCo aC	3.5 ± 1.5	7.8 ± 2.0	2.1 ± 0.1
PtCoN bC	5.3 ± 1.7	1.5 ± 0.6	-
PtCoN aC	4.5 ± 1.7	3.0 ± 0.4	1.6 ± 0.3
AuPtCoN bC	5.2 ± 1.8	1.0 ± 0.4	-
AuPtCoN aC	4.2 ± 1.6	1.5 ± 0.9	0.2 ± 0.2

The errors given for average diameters and Pt loss are standard deviations while the errors for the Pt/Co-ratios are standard errors.

4.2 Range Extended EXAFS with a BCLA

While nanoparticles containing both platinum and gold are interesting systems^{24–28}, elucidating their structures with EXAFS is difficult because the L_{III}-edges of Pt and Au are very close to each other (11.56 keV for Pt, 11.92 keV for Au). One possible solution is to measure the K-edge instead of the L_{III}-edge, because the K-edges of Pt and Au are separated by more than 2 keV.²⁹ Another solution is the so called range-extended XAFS method to filter out the fluorescence from the Au L_{III}-edge with an energy filter.^{30–32} However, the normal range-extended methods require a large high energy resolution fluorescence detection (HERFD) setup and thus HERFD experiments are limited to a few special beam lines dedicated for this kind of measurement. Here we propose a low-cost, flexible and simple range-extension method using a BCLA, which extends the possibility of the range extended methods to normal XAFS beam lines in high-brilliance synchrotron facilities. Figure 1 shows the Pt L_{III}-edge EXAFS of AuPtCoN/HOPG. No Au edge is observed in the Pt spectrum, demonstrating our ability to filter out the Au edge.

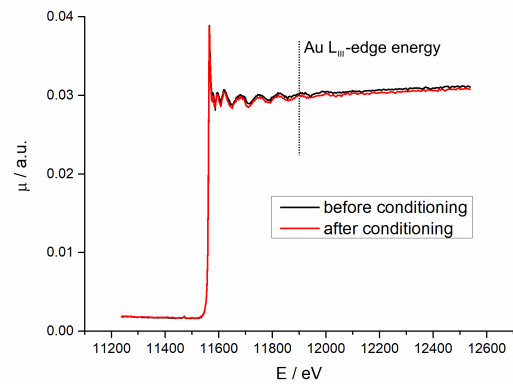


Fig. 2 Deglitched Pt L_{III}-edge EXAFS data for AuPtCoN nanoparticles; the Au L_{III}-edge at 11920 eV has been successfully removed by the BCLA

4.3 Edge Jump Height Analysis

The Pt L_{III}-edge jump height of the data decreases as a result of the electrochemical conditioning for all samples. The relative magnitude of this loss is proportional to the amount of lost Pt. Moreover, since the same sample is treated under *in situ* conditions, the edge height difference can be directly compared before and after conditioning. Thus, the reduction in the Pt L_{III}-edge jump is discussed here to estimate the stability of the different nanoparticles. Figure S9 in the SI shows an example for the linear fits before and after the Pt L_{III}-edge that are used to calculate the edge jump. Table 1 summarizes the reduction in the Pt L_{III}-edge, with the Pt loss calculated according to equation 3, relative to the value before conditioning. As expected, the conditioning treatment reduced the Pt content in the order Pt > PtCo > PtCoN > AuPtCoN, i.e. the loss of Pt is largest for pure Pt NPs and smallest for AuPtCoN. It should be stressed, that for the alloy NPs, i.e. all samples except the pure Pt, the Pt L_{III}-edge jump reduction is not necessarily a measure of the overall nanoparticle stability because Co can be dissolved instead of Pt. Instead, the reduction in the Pt L_{III}-edge jump is an indicator of the NPs' tendency to lose Pt.

$$Pt\ loss(\%) = \frac{(edge\ height\ bc) - (edge\ height\ ac)}{edge\ height\ bc} \times 100 \quad (3)$$

4.4 Simple EXAFS fitting analysis

The EXAFS spectra are fitted using the EXAFS formula as described above. Although the Co K-edge was measured, the quality of the data is not good enough for EXAFS analysis due to the thickness of the HOPG window which reduces the incident and fluorescence X-ray intensity, in the Co K-edge measurement. Here, we only perform EXAFS analysis on the Pt L_{III}-edge spectra. The EXAFS spectra of all samples are presented in Figure 3. Figure 3A shows the data in k-space, demonstrating the decrease in signal to noise ratio at high k. Figure 3B shows the data in R-space, i.e. the Fourier transform, with the main-peak corresponding to the Pt-Pt path showing up between 2 Å and 3 Å.

An estimate of the number of independent data points N_{ind} can be made using the Nyquist-criterion:

$$N_{ind} = \frac{2\Delta k\Delta R}{\pi} \quad (4)$$

$\Delta k = 9.25\ \text{\AA}^{-1}$ ($3\ \text{\AA}^{-1}$ to $12.25\ \text{\AA}^{-1}$) and $\Delta R = 1.75\ \text{\AA}$ ($1.5\ \text{\AA}$ to $3.25\ \text{\AA}$) results in 10.3 independent data points. Two scattering paths are used, a single scattering path between a platinum absorber and a platinum scatterer (Pt-Pt) and another path between a platinum absorber and a cobalt scatter (Pt-Co). Au neighbors are treated as Pt since the scattering from Au and Pt is nearly identical due to the similar atomic number. For each path, the coordination number N , the Debye-Waller factor σ^2 and the distance between absorber and scatterer r were fitted. This corresponds to six fit parameters, significantly less than the number of independent data points. ΔE_0 is fixed to a value of 7.5 eV as discussed above. The effect of changes in ΔE_0 on the bond distance r is used to estimate the errors for r and discussed in detail in the SI. The

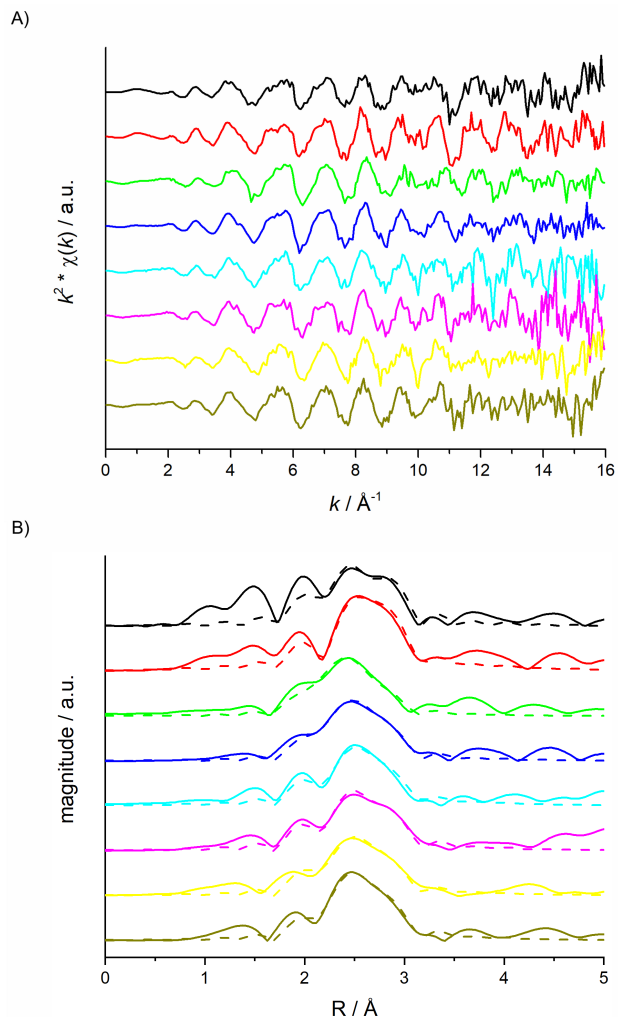


Fig. 3 Pt L_{III}-edge EXAFS data for all samples in k-space (A) and the Fourier-transform (B); solid lines correspond to experimental data while the dashed lines (only in B) show the fitted curves; from top to bottom: black – Pt bC, red – Pt ac, green – PtCo bC, blue – PtCo ac, teal – PtCoN bC, pink – PtCoN ac, yellow – AuPtCoN bC, ochre – AuPtCoN ac

SI also includes a detailed discussion of the statistical significance of the third decimal digit of the bond lengths. Table 2 shows the fitting results for all eight samples with the standard deviations from least squares fitting for N and σ^2 . The Pt-Pt distances in the pure Pt NPs ($2.75 \pm 0.02\ \text{\AA}$ and $2.75 \pm 0.01\ \text{\AA}$ for bC and ac, respectively) remain unchanged after electrochemical conditioning and are smaller than the Pt-Pt distance in bulk Pt ($2.775\ \text{\AA}$).³³ The Pt-Pt bond length in the alloy nanoparticles is even shorter than that in the pure Pt nanoparticles. It is the shortest in the PtCo NPs before conditioning ($2.71 \pm 0.04\ \text{\AA}$). Electrochemical conditioning increases the Pt-Pt bond length for all NPs containing Co, although the changes in bond lengths of PtCoN and AuPtCoN are only in the third decimal digit, not shown in Table 2. The reason for the significantly reduced bond length in PtCo bC is the alloying of platinum and cobalt; PtCo alloys are known to have shorter Pt-Pt bond lengths than pure Pt.³⁴ The significant increase in the Pt-Pt bond length for PtCo ac is thus a result of dealloying: a lot of Co is lost in the electrochemical conditioning and Pt is segreg-

gated. The errors for coordination numbers N and Debye-Waller factors σ^2 are large because the two parameters are directly correlated in the EXAFS equation (eq. 1). Usually, we carry out the EXAFS analysis for both edges (Pt and Co) simultaneously, satisfying the relevant physical constraints to reduce the correlation between N and σ^2 .^{20,34} The strong correlation between σ^2 and N leads to an unphysical value of $N_{total} = N(Pt - Pt) + N(Pt - Co)$ for the PtCoN aC sample. For this sample, simple EXAFS fitting yields a value of 13.3 for N_{total} , which is more than the maximum number of nearest neighbors in a closed packed structure (12). While the correlation between σ^2 and N is most obvious for the PtCoN aC sample, the two variables are correlated for all samples. Thus, additional analysis is required to correctly identify the values of σ^2 for the various samples and the corresponding other EXAFS fit parameters. A more detailed discussion of the correlation between N and σ^2 can be found in the SI.

4.5 Model Building Analysis(MBA)

In order to improve the accuracy of the EXAFS analysis and to determine structural models for the nanoparticle samples we perform an extensive comparison of fits to the EXAFS spectra and structural models. Because of the inability of the simple EXAFS fits, described above, to reliably determine the Debye Waller-factors $\sigma^2(Pt - Pt)$ and $\sigma^2(Pt - Co)$, we study, for each sample, a large number of EXAFS fits with varying Debye Waller-factors. The respective EXAFS fits and their corresponding fit parameters are described in the SI as 2D mapping and 2D filtering and displayed in Figures S12-S62. Also in the SI, the reader can find a detailed description of the determination of normalization factors, used in equation 5 below. For each sample, the multitude of EXAFS fits obtained is compared with structural models. In the following we describe in detail the construction of the structural models, the comparison between EXAFS fits and structural models, the identification of physically reasonable, statistically significant pairs of EXAFS fits and structural models and the subsequent determination of EXAFS parameters and average structural models for the samples.

4.5.1 Construction of structural models.

Structural models for PtCo, PtCoN and AuPtCoN nanoparticles are constructed. To generate the structures and calculate statistics we wrote a computer program. The workflow of the program is described in Figure 4. The average particle diameters obtained through STEM (see Table 1) are used as the NP-diameters for the respective samples. Several different types of structural models are explored: completely random NPs, NPs with a Co-core and a random PtCo shell, NPs with a random Pt-Co core and a Pt shell and NPs with a Co-core, a random intermediate PtCo phase and a Pt shell. No well-ordered PtCo phases are considered, as XRD measurements show no indication of ordered PtCo phases.¹⁶ For structural models of the Au-containing NPs Au is added on the surface of the nanoparticles, because STEM-EDS indicates that Au is located on the surface of the NPs. For all NPs containing nitrogen, one N atom is added in an interstitial site for each Co atom in the Co-core, visualizing the formation of CoN. X-ray photoelectron spectroscopy demonstrates a change to the Co 2p region as

a result of the addition of nitrogen which is indicative of the formation of cobalt nitride.¹⁶ XPS does not indicate any change to the Pt 4f peak and thus we do not assume formation of PtN and consequently do not add nitrogen atoms next to Pt. The addition of nitrogen to the model images is for visualization purposes only. Our EXAFS analysis and MBA do not give any direct information on the existence/absence of N in the nanoparticles. Pt/Co-ratios (over the entire particle) are varied within the error given by the STEM-EDS measurements. This led to hundreds or thousands of structural models for each sample. One may find additional details in the SI.

4.5.2 Comparison of EXAFS fits and structural models.

In order to determine, which EXAFS fits correspond to physically reasonable model structures, each EXAFS fit is compared to each model structure generated for that sample using two parameters: 1) **The local Pt/Co-ratio**, $\alpha = N(Pt - Pt)/N(Pt - Co)$. α describes the environment around Pt-atoms, for the EXAFS fits it is simply calculated as stated in the last sentence; for the structural models this calculation is performed for each Pt-atom in the structure and the average of the values for all Pt-atoms in a structural model gives α_{Model} . This should not be confused with the Pt/Co-ratio over the entire cluster, which is determined with STEM-EDS and used in the construction of the models. 2) **The total number of nearest neighbors** N_{total} as defined above, for simplicity's sake simply called N in equation 5:

$$R_{comp} = \frac{(\alpha_{Model} - \alpha_{EXAFS})^2}{\delta\alpha_{EXAFS}} + \frac{(N_{Model} - N_{EXAFS})^2}{\delta N_{EXAFS}} \quad (5)$$

R_{comp} is an index describing the level of agreement between important parameters derived from both model structure and EXAFS fit. The squared differences between the parameters derived from model and EXAFS fit are normalized by their respective variances, δ , see the SI for information on how these are calculated. The sum of both of the quotients gives R_{comp} . In this way, every single EXAFS fit is compared to every single structural model (for the respective sample), giving between 27000 and 1.3 million such pairs per sample. These pairs are henceforth referred to as comparisons. The numbers of comparisons obtained in this way are listed in Table S1 in the SI.

4.5.3 Filtering of the comparisons of structural models and EXAFS fits.

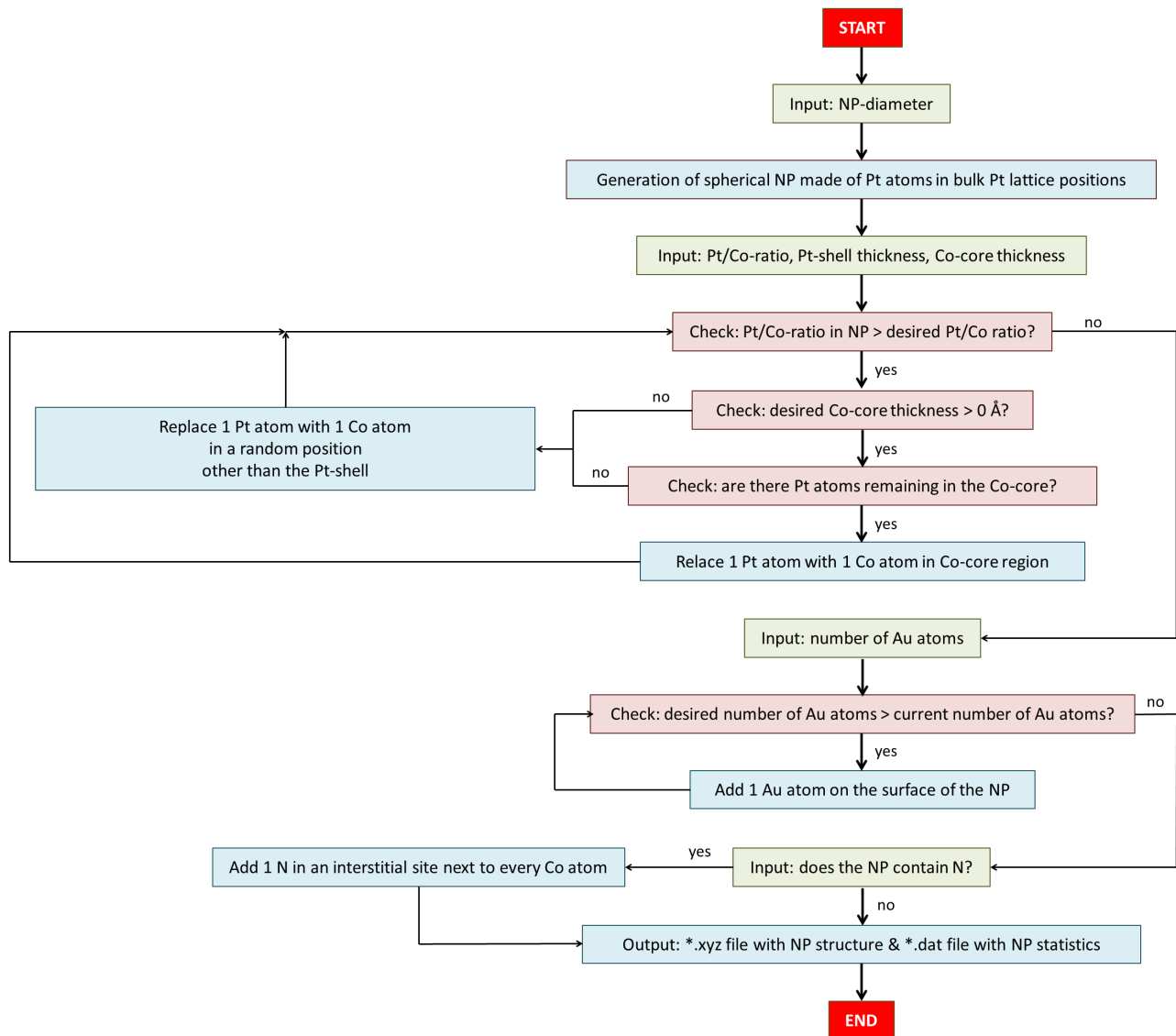
All of the comparisons between EXAFS fits and structural models are filtered with two criteria: 1) $R_{comp} < 2$ is required to only allow fits that correspond reasonably well to a physical model. The value of 2 corresponds to agreement of structural model and EXAFS fit within the errors of the EXAFS fit parameters. 2) The R-factor of the EXAFS fit is restricted to values smaller than or equal to two times the best fit R-factor, i.e. $R_{EXAFS} \leq 2 * R_{EXAFS,min}$. All comparisons that fulfill both conditions are used in the subsequent identification of EXAFS parameters and structural models.

4.5.4 Identification of EXAFS parameters and structural models.

To obtain EXAFS parameters and average structural models from the model building results, each parameter is averaged over all

Table 2 EXAFS Fitting Results

Sample	Path	N	$\sigma^2 / \text{\AA}^2$	$r / \text{\AA}$	R-factor
Pt bC	Pt-Pt	7.4 ± 1.4	0.0054 ± 0.0010	2.75 ± 0.02	4.9 %
Pt aC	Pt-Pt	9.8 ± 1.0	0.0051 ± 0.0010	2.75 ± 0.01	1.5 %
PtCo bC	Pt-Pt	6.7 ± 2.1	0.0068 ± 0.0019	2.71 ± 0.04	2.0 %
	Pt-Co	3.6 ± 1.6	0.0097 ± 0.0040	2.63 ± 0.06	
PtCo aC	Pt-Pt	8.1 ± 2.4	0.0061 ± 0.0017	2.74 ± 0.03	1.8 %
	Pt-Co	1.8 ± 1.3	0.0060 ± 0.0054	2.64 ± 0.08	
PtCoN bC	Pt-Pt	6.5 ± 1.8	0.0048 ± 0.0015	2.74 ± 0.02	1.7 %
	Pt-Co	3.3 ± 2.1	0.0141 ± 0.0074	2.65 ± 0.11	
PtCoN aC	Pt-Pt	9.6 ± 1.8	0.0062 ± 0.0012	2.74 ± 0.02	1.1 %
	Pt-Co	3.7 ± 4.7	0.0231 ± 0.0177	2.70 ± 0.13	
AuPtCoN bC	Pt-Pt	7.7 ± 1.9	0.0056 ± 0.0013	2.74 ± 0.02	1.6 %
	Pt-Co	2.1 ± 1.4	0.0092 ± 0.0058	2.64 ± 0.14	
AuPtCoN aC	Pt-Pt	8.9 ± 2.3	0.0059 ± 0.0015	2.74 ± 0.03	1.7 %
	Pt-Co	1.6 ± 1.4	0.0064 ± 0.0069	2.67 ± 0.13	

**Fig. 4** Flow-diagram explaining the workflow of the computer program used to generate NP structures and calculate statistics.

comparisons that pass the filtering for the respective sample. The errors are calculated by taking the standard deviations of the parameters.

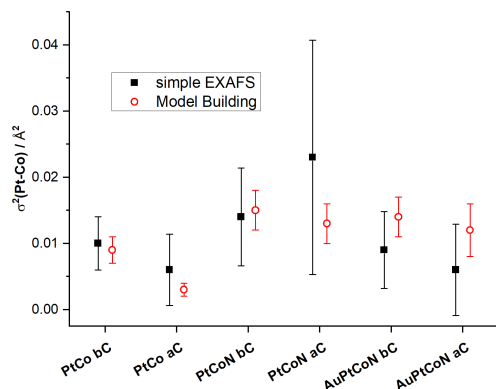


Fig. 5 $\sigma^2(Pt-Co)$ with error bars obtained with simple EXAFS fitting (black squares) and MBA (red open circles)

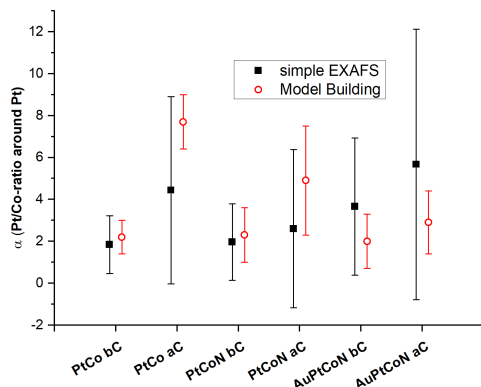


Fig. 6 α , Pt/Co-ratio around Pt with error bars obtained with simple EXAFS fitting (black squares) and MBA (red open circles).

4.5.5 Results of the MBA

Graphs of $\sigma^2(Pt-Co)$ and α , comparing the results of the MBA with those from simple EXAFS are shown in Figures 5 and 6 respectively, graphs of $\sigma^2(Pt-Pt)$, N_{total} , $r(Pt-Pt)$ and $r(Pt-Co)$ are presented in the SI, Figures S63 to S66. A table with detailed results for all EXAFS parameters is provided in Table S2 in the SI. Since r is correlated with ΔE in the EXAFS equation, the variations in σ^2 (and consequently N), that are central to the MBA, do not have any influence on r . As a result, $r(Pt-Pt)$ and $r(Pt-Co)$ have almost identical values and errors in the MBA and the simple EXAFS.

For $\sigma^2(Pt-Co)$, the MBA yields significantly different results than simple EXAFS. The errors for $\sigma^2(Pt-Co)$ for all six Co-containing samples are drastically reduced with MBA. For PtCo, PtCoN and AuPtCoN, conditioning leads to a reduction in $\sigma^2(Pt-Co)$. Importantly, for PtCoN ac, $\sigma^2(Pt-Co)$, which is erroneously

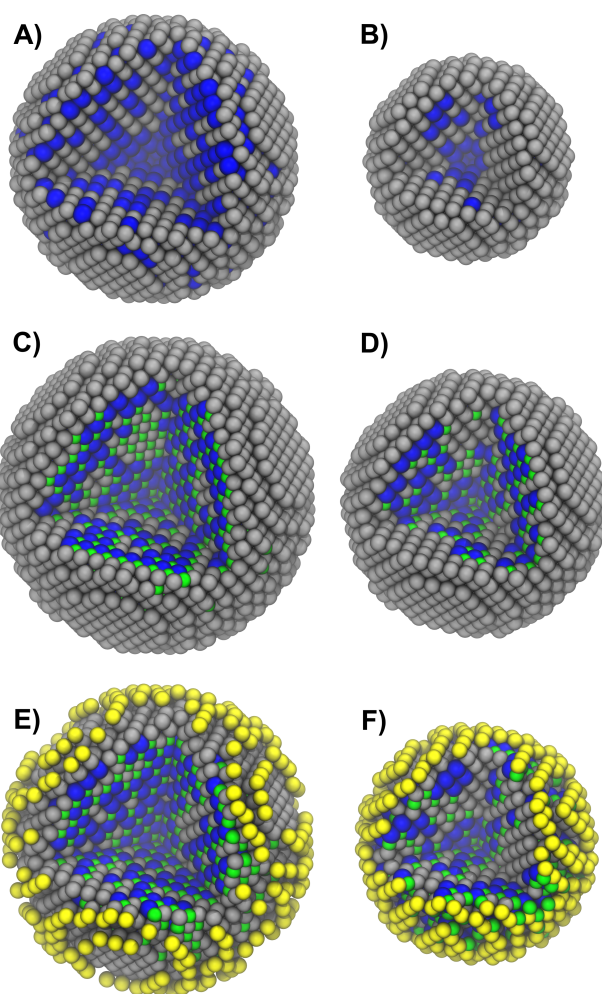


Fig. 7 Visualizations of the results of the MBA; A) PtCo bc, B) PtCo ac, C) PtCoN bc, D) PtCoN ac, E) AuPtCoN bc, F) AuPtCoN ac. Orange: Pt, blue: Co, green: N, Yellow: Au

large with a value of 0.023\AA^2 in simple EXAFS, has a reasonable value of 0.013\AA^2 in the MBA.

The Pt/Co-ratios around Pt, α , can be determined much more accurately from the MBA than from simple EXAFS, as displayed in Figure 6. They increase as a result of electrochemical conditioning for all three samples with the increase being most significant for PtCo and almost negligible for AuPtCoN. This corresponds to the improved stability, more precisely, the increased ability to stabilize Co in the order PtCo < PtCoN < AuPtCoN. The segregation, i.e. separation of Pt and Co caused by the formation of a Pt-shell is another factor in this, as discussed below.

The structural parameters resulting from the MBA are listed in Table 3 and corresponding model images are presented in Figure 7. All six Co-containing samples display a Pt-shell on the outside and a Co-core on the inside with a mixed Pt-Co-phase in between. The thickness of the Pt-shell increases after electrochemical conditioning; this is a result of Co being leached more easily than Pt. While these general trends hold for the three different compositions, PtCo, PtCoN and AuPtCoN, it is important to point out the differences between them.

Table 3 Model parameters resulting from the MBA with standard deviations

Sample	Pt/Co-ratio	Pt-shell thickness / Å	Co-core diameter / Å	Au atoms
PtCo bC	1.7 ± 0.2	2.5 ± 1.6	5.0 ± 3.2	-
PtCo aC	7.4 ± 1.1	2.9 ± 1.9	2.8 ± 2.1	-
PtCoN bC	1.5 ± 0.3	2.8 ± 1.9	5.0 ± 3.2	-
PtCoN aC	3.0 ± 0.3	3.7 ± 2.4	5.0 ± 3.2	-
AuPtCoN bC	1.0 ± 0.3	2.3 ± 1.6	5.0 ± 3.2	404 ± 259
AuPtCoN aC	1.6 ± 0.5	2.0 ± 1.5	5.0 ± 3.2	414 ± 260

For PtCo, the Pt-shell before conditioning is very thin and could be a result of some dissolution of Co under the measurement conditions. Electrochemical conditioning of the PtCo nanoparticles leads to significant dissolution of Co and thus the largest increase in the Pt/Co-ratio out of all the samples. This is true for the Pt/Co-ratio over the entire molecule (as measured with STEM-EDS and used in the MBA) and the local Pt/Co-ratio, α . The large loss of Co also leads to the biggest reduction in size, compared with PtCoN and AuPtCoN.

The PtCoN sample shows a pronounced Pt-shell, already before electrochemical conditioning. This is, most likely, a result of the formation of a cobalt-nitride core. The Pt-shell grows thicker during electrochemical conditioning and the particles shrink due to loss of material, although to a lesser degree than in the PtCo sample.

The AuPtCoN sample shows the least degree of change during electrochemical conditioning. The thickness of the Pt-shell is almost unchanged. The error for the amount of Au-atoms on the NPs surfaces is very large. Due to the added parameter (the number of Au atoms) in the model building, the results for these samples are less reliable than for the PtCo and PtCoN samples. Measurements of the Au L_{III}-edge are necessary to determine the structures of the Au-containing nanoparticles with higher accuracy in the future. For this, the sensitivity of the BCLA + BI-XAFS method needs to be increased by a factor of ten due to the much smaller amount of Au.

The MBA indicates that the Co-core radius is 5 Å for all samples other than PtCo ac. However, this result is not so reliable, corresponding to the average of the eleven Co-core radii from 0 Å to 10 Å that are used in the model building. Further studies of the Co K-edge are necessary to allow reliable determination of the Co-core sizes. For this purpose we have to develop a very thin graphene window.³⁵

4.6 Relationship between ORR activity and Pt-Pt bond length

Table 4 compares the ORR activity^{17,18} with the Pt-Pt bond length for the samples aC. All alloy samples have much higher activities than the pure Pt NPs, both in mass activity and specific activity. At the same time, the Pt-Pt bond length in the alloy NPs is shortened relative to pure Pt NPs.

A previous study by Kaito et al. investigated the relationship between Pt-Pt bond length and area specific ORR activity and found an increase in the activity with decreasing $r(Pt - Pt)$.³⁴ Within the error bars our results match the linear relationship they obtained. This is despite the fact that the preparation methods used in that study by Kaito et al. and in our present work are very different.

They used wet impregnation to form the nanoparticles on powdered carbon support and prepared samples for catalytic testing by coating glassy carbon with inks prepared from the nanoparticles. In our case the NPs are created by arc-plasma deposition on a flat surface (HOPG). The fact that both studies show the same relationship between $r(Pt - Pt)$ and specific ORR activity despite these different preparation methods, and, consequently, rather different catalysts, is an indication that a universal relation, regardless of substrate morphology, between area specific ORR activity and Pt-Pt bond length exists for Pt-alloy nanoparticles. A graph showing this linear relationship can be found in the Supporting Information, Figure S67.

The increased mass activity of PtCoN relative to PtCo corresponds to more pronounced formation of Pt-shells in the N-containing sample. The lower mass activity for AuPtCoN, relative to PtCoN, most likely indicates the partial occupation of active sites on the NP surface by Au. N-incorporation and Au-decoration both significantly improve the stability of the NPs. The mass activity of AuPtCoN samples can be optimized by changing the amount of Au to achieve an optimal balance between stability and activity.

5 Conclusion

We have carried out BCLA + BI-XAFS measurements on Pt containing nanoparticles, prepared by APD on a flat HOPG surface, with good S/N. We can successfully remove the Au L_{III}-edge using a BCLA. We have obtained good S/N ratios in Pt L_{III}-edge EXAFS spectra of as little as $1 \times 10^{15} \text{cm}^{-2}$ Pt on HOPG. We do not obtain useable Co K-edge spectra in the BCLA + BI-XAFS experiments due to the HOPG window thickness. The Pt L_{III} single edge analysis leads to a strong correlation between $N(Pt - Co)$ and $\sigma^2(Pt - Co)$. In order to overcome this problem we have developed a MBA, which allows us to obtain physically reasonable fitting results. Consequently, we can increase the accuracy of the EXAFS fitting parameters significantly and determine structural models for PtCo, PtCoN and AuPtCoN nanoparticles before and after electrochemical conditioning. We have shown that the nanoparticles have a Pt-shell and Co-core with a mixed Pt/Co-phase in between. The Pt-shell grows as a result of electrochemical conditioning, but the Au-covered NPs are so stable that no growth of the Pt-shell is observed. Our results are in good agreement with STEM-EDS measurements.^{16,18} We have confirmed the universal linear correlation between the specific activity and Pt-Pt bond distance. This work introduces an analytical method which we call MBA. It allows us to carry out rational analysis to study multimetallic nanoparticles using only a single absorption edge. Because the accuracy of the structural parameters determined with just one absorption edge is limited, we plan to improve

Table 4 Comparison between ORR activity and Pt-Pt bond length, as determined from the MBA, for the nanoparticles aC

Sample	r(Pt-Pt) / Å	Mass Activity / A/mg	Area Specific Activity / mA/cm ²
Pt ac*	2.75 ± 0.01	0.84 ± 0.04	0.63 ± 0.03
PtCo aC	2.74 ± 0.03	1.12 ± 0.15	1.04 ± 0.14
PtCoN aC	2.74 ± 0.02	1.65 ± 0.17	0.99 ± 0.10
AuPtCoN aC	2.74 ± 0.02	1.15 ± 0.11	1.09 ± 0.10

* The Pt-Pt distance for the pure Pt particles is taken from the simple EXAFS analysis, as no model building was performed for this sample.

these measurements by optimizing the HOPG substrate thickness to successfully obtain Co K-edge data and also measure the Au L_{III}-edge. The combination of three absorption edges into the EXAFS fits will significantly increase the accuracy of the results. Our novel method should be able to help solve the structure of multimetallic nanoparticles investigated by EXAFS for a variety of systems and could even be expanded to consider nanoparticle shape.

Conflicts of interest

There are no conflicts to declare.

Acknowledgements

Felix E. Feiten gratefully acknowledges financial support from the Japanese Society for the Promotion of Science and the Alexander von Humboldt Foundation. This work was supported by the NEDO PEFCs project and JSPS Grant-in-Aids for Scientific Research A 20H00367. The EXAFS measurements were carried out with approval from JASRI (2016B7905, 2017B7905, 2019A7904, 2019B7904).

Notes and references

- 1 J.-H. Wee, *Renewable and Sustainable Energy Reviews*, 2007, **11**, 1720 – 1738.
- 2 R. F. Service, *Science*, 2009, **324**, 1257–1259.
- 3 H. A. Gasteiger, S. S. Kocha, B. Sompalli and F. T. Wagner, *Applied Catalysis B: Environmental*, 2005, **56**, 9 – 35.
- 4 Y. Shao-Horn, W. C. Sheng, S. Chen, P. J. Ferreira, E. F. Holby and D. Morgan, *Topics in Catalysis*, 2007, **46**, 285–305.
- 5 E. F. Holby, W. Sheng, Y. Shao-Horn and D. Morgan, *Energy Environ. Sci.*, 2009, **2**, 865–871.
- 6 F. Hasché, M. Oezaslan and P. Strasser, *ChemCatChem*, 2011, **3**, 1805–1813.
- 7 S. Cherevko, G. P. Keeley, S. Geiger, A. R. Zeradjanin, N. Hodnik, N. Kulyk and K. J. J. Mayrhofer, *ChemElectroChem*, 2015, **2**, 1471–1478.
- 8 J. Greeley, I. E. L. Stephens, A. S. Bondarenko, T. P. Johansson, H. A. Hansen, T. F. Jaramillo, J. Rossmeisl, I. Chorkendorff and J. K. Nørskov, *Nature Chemistry*, 2009, **1**, 552–556.
- 9 D. Wang, H. L. Xin, R. Hovden, H. Wang, Y. Yu, D. A. Muller, F. J. DiSalvo and H. D. Abruña, *Nature Materials*, 2012, **12**, 81 EP –.
- 10 M. Heggen, M. Oezaslan, L. Houben and P. Strasser, *The Journal of Physical Chemistry C*, 2012, **116**, 19073–19083.
- 11 A. Rabis, P. Rodriguez and T. J. Schmidt, *ACS Catalysis*, 2012, **2**, 864–890.
- 12 N. Todoroki, T. Kato, T. Hayashi, S. Takahashi and T. Wadayama, *ACS Catalysis*, 2015, **5**, 2209–2212.
- 13 Y. Shao, G. Yin and Y. Gao, *Journal of Power Sources*, 2007, **171**, 558 – 566.
- 14 J. Wu, X. Z. Yuan, J. J. Martin, H. Wang, J. Zhang, J. Shen, S. Wu and W. Merida, *Journal of Power Sources*, 2008, **184**, 104 – 119.
- 15 K. J. J. Mayrhofer, K. Hartl, V. Juhart and M. Arenz, *Journal of the American Chemical Society*, 2009, **131**, 16348–16349.
- 16 S. Takahashi, N. Takahashi, N. Todoroki and T. Wadayama, *ACS Omega*, 2016, **1**, 1247–1252.
- 17 S. Takahashi, H. Chiba, T. Kato, S. Endo, T. Hayashi, N. Todoroki and T. Wadayama, *Phys. Chem. Chem. Phys.*, 2015, **17**, 18638–18644.
- 18 S. Takahashi, N. Todoroki, R. Myochi, T. Nagao, N. Taguchi, T. Ioroi, F. E. Feiten, Y. Wakisaka, K. Asakura, O. Sekizawa, T. Sakata, K. Higashi, T. Uruga, Y. Iwasawa and T. Wadayama, *Journal of Electroanalytical Chemistry*, 2019, **842**, 1 – 7.
- 19 B. K. Teo, M. R. Antonio and B. A. Averill, *Journal of the American Chemical Society*, 1983, **105**, 3751–3762.
- 20 C.-R. Bian, S. Suzuki, K. Asakura, L. Ping and N. Toshima, *The Journal of Physical Chemistry B*, 2002, **106**, 8587–8598.
- 21 H. Uehara, Y. Uemura, T. Ogawa, K. Kono, R. Ueno, Y. Niwa, H. Nitani, H. Abe, S. Takakusagi, M. Nomura, Y. Iwasawa and K. Asakura, *Phys. Chem. Chem. Phys.*, 2014, **16**, 13748–13754.
- 22 Y. Wakisaka, D. Kido, H. Uehara, Q. Yuan, F. E. Feiten, S. Mukai, S. Takakusagi, Y. Uemura, T. Yokoyama, T. Wada, M. Uo, O. Sekizawa, T. Uruga, Y. Iwasawa and K. Asakura, *The Chemical Record*, 2019, **19**, 1157–1165.
- 23 B. Ravel and M. Newville, *Journal of Synchrotron Radiation*, 2005, **12**, 537–541.
- 24 M.-L. Wu, D.-H. Chen and T.-C. Huang, *Chemistry of Materials*, 2001, **13**, 599–606.
- 25 H. Lang, S. Maldonado, K. J. Stevenson and B. D. Chandler, *Journal of the American Chemical Society*, 2004, **126**, 12949–12956.
- 26 C. Song, Q. Ge and L. Wang, *The Journal of Physical Chemistry B*, 2005, **109**, 22341–22350.
- 27 P. Hernández-Fernández, S. Rojas, P. Ocón, J. L. Gómez de la Fuente, J. San Fabián, J. Sanza, M. A. Peña, F. J. García-García, P. Terreros and J. L. G. Fierro, *The Journal of Physical Chemistry C*, 2007, **111**, 2913–2923.
- 28 J. Suntivich, Z. Xu, C. E. Carlton, J. Kim, B. Han, S. W. Lee, N. Bonnet, N. Marzari, L. F. Allard, H. A. Gasteiger, K. Hamad-Schifferli and Y. Shao-Horn, *Journal of the American Chemical Society*, 2013, **135**, 7985–7991.

- 29 T. Kaito, H. Mitsumoto, S. Sugawara, K. Shinohara, H. Uehara, H. Ariga, S. Takakusagi, Y. Hatakeyama, K. Nishikawa and K. Asakura, *The Journal of Physical Chemistry C*, 2014, **118**, 8481–8490.
- 30 P. Glatzel, F. M. F. de Groot, O. Manoilova, D. Grandjean, B. M. Weckhuysen, U. Bergmann and R. Barrea, *Phys. Rev. B*, 2005, **72**, 014117.
- 31 J. Yano, Y. Pushkar, P. Glatzel, A. Lewis, K. Sauer, J. Messinger, U. Bergmann and V. Yachandra, *Journal of the American Chemical Society*, 2005, **127**, 14974–14975.
- 32 H. Asakura, N. Kawamura, M. Mizumaki, K. Nitta, K. Ishii, S. Hosokawa, K. Teramura and T. Tanaka, *J. Anal. At. Spectrom.*, 2018, **33**, 84–89.
- 33 Y. Waseda, K. Hirata and M. Ohtani, 1975, **7**, 221–226.
- 34 T. Kaito, H. Tanaka, H. Mitsumoto, S. Sugawara, K. Shinohara, H. Ariga, H. Uehara, S. Takakusagi and K. Asakura, *The Journal of Physical Chemistry C*, 2016, **120**, 11519–11527.
- 35 T. Ma, K. Miyazaki, H. Ariga, S. Takakusagi and K. Asakura, *Bulletin of the Chemical Society of Japan*, 2015, **88**, 1029–1035.